ACCOUNTS
of chemical research

Article

Visualizing Solution-Phase Reaction Dynamics with Time-Resolved X-ray Liquidography

Hyotcherl Ihee

More About This Article

Additional resources and features associated with this article are available within the HTML version:

- Supporting Information
- Access to high resolution figures
- Links to articles and content related to this article
- Copyright permission to reproduce figures and/or text from this article

View the Full Text HTML

ACS Publications
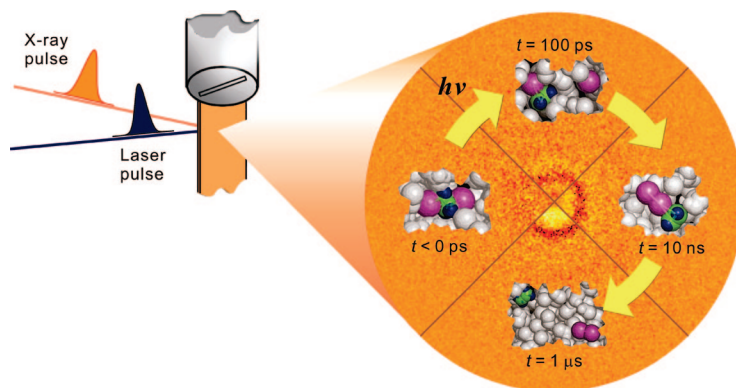### High quality. High impact.

Visualizing Solution-Phase Reaction Dynamics with Time-Resolved X-ray Liquidography

HYOTCHERL IHEE

Center for Time-Resolved Diffraction, Department of Chemistry, KAIST, Daejeon 305-701, Republic of Korea

CONSPECTUS

Most chemical reactions occur in solution, and complex interactions between solute and solvent influence the rich chemistry of these processes. To track time-dependent processes in such reactions, researchers often use time-resolved spectroscopy. In these experiments, an optical pulse (pump) initiates a reaction, and another time-delayed optical pulse (probe) monitors the progress of the reaction. However, because of the wavelength range of the probe light used in these experiments, from infrared to ultraviolet, researchers cannot directly determine detailed structural information such as the bond lengths and bond angles of reaction intermediates. In addition, not all intermediates might be sensitive to the spectroscopic signal chosen for the experiment.

This Account describes time-resolved X-ray liquidography (TRXL), a technique that overcomes these problems. In this technique, we replace the optical probe with the diffraction of hard X-ray pulses emitted from a synchrotron source. In TRXL, diffraction signals are sensitive to all chemical species simultaneously. In addition, each chemical species has a characteristic diffraction signal, a fingerprint, that we calculate from its three-dimensional atomic coordinates. Because, X-rays scatter from all atoms in the solution sample, including both the solute and the solvent, the analysis of TRXL data can track not only the reaction pathways of the solute molecules but also the solvent behavior and the solute—solvent arrangement, thus providing a global picture of the reactions.

We have used TRXL to study structural dynamics and spatiotemporal kinetics of many molecular systems including diatomic molecules, haloalkanes, organometallic complexes, and protein molecules over timescales from picoseconds to milliseconds. We have observed that TRXL data adds to and, in some cases, contradicts results from time-resolved spectroscopy. For example, TRXL has shown that the reaction intermediates upon C—I bond dissociation in $C_2H_4I_2$ and $C_2F_4I_2$ have completely different structures and corresponding subsequent reaction pathways, underscoring the dramatic effect of the fluorine substitution. We have also used TRXL to identify a new reaction intermediate of the photolysis of $Ru_3(CO)_{12}$ that has no bridging carbonyl groups. Though not detected by time-resolved infrared spectroscopy, this intermediate predominates based on the TRXL data. In looking at the quaternary conformational changes of hemoglobin, TRXL analysis suggests a faster transition than was suggested by optical spectroscopy.

The time resolution of TRXL is currently limited by the X-ray pulse width available from synchrotron sources (∼100 ps). The resolution should improve to 100 fs or better with X-ray free electron lasers. With this higher resolution, real time observation of ultrafast chemical events such as bond-breaking and bond-making will be possible.

Introduction

Most chemical and biologically relevant reactions occur in solution, and solution-phase reactions exhibit rich chemistry due to the solute−solvent interplay. The understanding of reaction mechanisms and molecular functions in such reactions requires detailed knowledge of time-dependent reaction processes. To track such processes, various time-resolved spectroscopic tools have been developed.[1−6] In a typical experiment, an optical pulse (pump) is used to trigger a reaction, and another time-delayed optical pulse (probe) is used to investigate the progress of the reaction. In most cases, however, detailed structural information such as bond lengths and angles of reaction intermediates are difficult to obtain from such methods apart from a select few cases. We are faced with this deficit because the signals of typical time-resolved optical spectroscopy using frequencies in the range of vibrational to valence electronic excitations are generally not a direct function of the molecular structure in terms of atomic coordinates.

Substituting the optical probe pulses in time-resolved optical spectroscopy with hard X-rays (∼1 Å) offers a more direct means to investigate the structural dynamics in molecular reactions.[7−22] For example, all the atomic positions in a protein can be tracked during its biological function by time-resolved X-ray crystallography,[22] but producing single crystals of proteins is a prerequisite. However with the recent advent of time-resolved liquid-phase X-ray diffraction (scattering), transient molecular structure can be captured even in a liquid sample without any crystallization.[10−21] The diffraction from a disordered sample is often called diffuse scattering to distinguish it from the Bragg diffraction peaks of a well-ordered system. For this reason, liquid X-ray diffraction has also been called liquid X-ray scattering, and in this Account, both terms are used interchangeably. Time-resolved X-ray diffraction of solution samples has been called by many different names, for example, time-resolved liquid X-ray diffraction, transient X-ray diffraction, and ultrafast (or time-resolved) X-ray solution scattering. To emphasize that structural information about transient chemical species can be obtained from the liquid phase and to avoid the ambiguity of diffraction versus scattering, our group prefers to call this methodology "time-resolved X-ray liquidography" (TRXL). Here, the term "liquidography" is introduced by analogy to crystallography where the structural information is obtained from the crystalline phase. One caveat is that due to the orientational averaging from randomly oriented molecules and the lack of the crystal periodicity in liquid, liquidography offers much less information content for liquid than crystallography does for single crystals and even for polycrystalline samples.

In terms of structure analysis, TRXL offers advantages over time-resolved spectroscopy because the diffraction signal of a molecule can be readily calculated from the three-dimensional atomic coordinates of the molecule. Each chemical species has its own characteristic diffraction pattern, which can therefore be used to monitor the time propagation of its concentration. In practice, quantum calculations generally yield more accurate molecular structures than energy levels and spectra, thereby adding an extra advantage to TRXL.

Since X-rays scatter from all atoms in a solution sample, including both the solute and solvent, the diffraction signal can be decomposed to three contributions: (1) the solute-only term due to diffraction changes in the internal solute structure, (2) the solute−solvent cross term (also called the cage term) caused by diffraction changes in interatomic distances between solute−solvent pairs, and (3) the solvent-only term (hydrodynamics) from the scattering change in the bulk solvent due to the solvent temperature and density changes caused by the heat transferred from photon-absorbing solute molecules. Data collection and analysis of such a complicated signal is not trivial, but recent years have witnessed the birth and great advances of TRXL thanks to technological developments in synchrotron beamlines and advancements of theory and data analysis combining quantum calculation, molecular dynamics (MD) simulation, and global fitting analysis. In this Account, we summarize such advances.

Experiment

The experimental setup is schematically illustrated in Figure 1. It comprises a sample cell system, a pulsed laser system to excite the sample, a pulsed synchrotron source to produce ultrashort X-ray pulses to scatter from the sample, a synchronized high-speed chopper that selects single X-ray pulses and an integrating charge-coupled device (CCD) area detector.

A solution of 0.5−100 mM is circulated through an open-jet sapphire nozzle to provide a liquid sheet directly exposed to the laser/X-ray beams. The molecules in the jet are excited by a laser pulse from a femtosecond laser system synchronized with the X-ray pulses. The laser beam with an energy of 15−100 μJ depending on the excitation wavelength is focused to a 0.12×0.12 mm^2 spot. After excitation of the sample with the laser pulse, time-delayed X-ray pulses, generated by placing an undulator in the path of electron bunches and focused by a torroidal mirror, are delivered to the sample to a spot size of 0.1×0.06 mm^2 and scatter, thereby carrying time-dependent structural information in the resulting
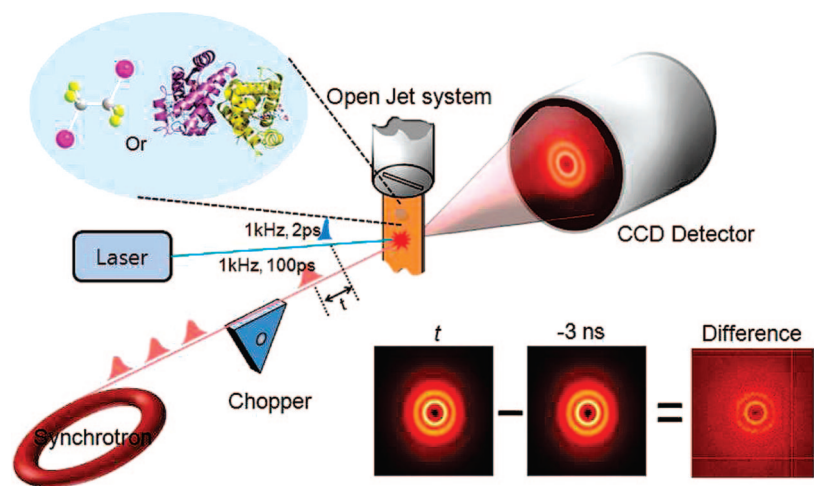
FIGURE 1. Schematic of the experimental setup for time-resolved X-ray liquidography. The liquid jet is irradiated by an optical laser pulse. After a well-defined time delay (t), the X-ray pulses generated by a synchrotron and selected by a high-speed chopper are sent to the sample and scattered. The reference diffraction data collected at -3 ns is subtracted from the diffraction data collected at positive time delays to extract the structural changes only.

scattered diffraction patterns. The X-ray spectrum is usually peaked at $\sim$18 keV and has a $\sim$3% bandwidth. This polychromatic rather than monochromatic X-ray beam is used to gain a high flux of X-ray photons. The polychromaticity affects the diffraction pattern by smearing out the oscillation features, but the 3% bandwidth is not large enough to seriously deteriorate them. In fact, if the X-ray spectrum had Gaussian distribution rather than asymmetric distribution with a long tail, the smearing would be even much less. The polychromaticity of the X-ray beam has to be taken into account when a theoretical diffraction curve is compared with the experimental diffraction curve by weighting the X-ray wavelength spectrum into the theoretical diffraction curve. The temporal X-ray pulse width is $60-150$ ps depending on the operation mode of the synchrotron, and a single X-ray pulse typically contains $\sim10^9$ X-ray photons. The synchronization of laser and X-ray pulses is based on an RF master clock that drives the electron bunches in a synchrotron ring. For example, at ESRF, the electron bunches in the synchrotron rotate around a 844 m long ring in 2.82 μs (single-bunch mode), and thus X-ray pulses are emitted when the electron bunches travel through an in-vacuum undulator at a repetition rate of 355 kHz, a subharmonic of the RF master clock. The time delay is generated by controlling the arrival time of the laser pulses onto the sample. The RF master clock is amplified and enters a phase shifter to generate a time-delayed RF clock, whose frequency is further divided to match the repetition rate of the femtosecond oscillator ($\sim$88 MHz) and amplifier ($\sim$1 kHz). Whereas the fine-tuning of the time delay is accomplished by the phase shifter, a larger time delay ($>$10 ns) is achieved by delaying the clock triggering the pockel cell of the amplifier with a delay generator. A series of shutters and choppers including a high-speed chopper (Julich) spinning at the same frequency as the laser are used to select single X-ray pulses out of the pulse trains from the synchrotron. The scattered X-ray diffraction signal is recorded on an area detector such as a MarCCD. A typical exposure time is $\sim$5 s, and given 1 kHz repetition rate of the laser/X-ray beam, the detector receives 5×10^3 X-ray pulses ($\sim5 \times 10^{12}$ X-ray photons) per image. Diffraction data is collected for typically ten or more time delays (t) from -100 ps up to 1 μs (for example, -100 ps, 0 ps, 30 ps, 100 ps, 300 ps, 1 ns, 3 ns, 10 ns, 30 ns, 100 ns, 300 ns, and 1 μs). Each time delay is interleaved by a measurement for the unperturbed sample (typically at -3 ns).

Data Processing

The resulting two-dimensional diffraction images are radially integrated into one-dimensional intensity curves, $S(q,t)_{exp}$, as a function of the momentum transfer q ($q = (4\pi/\lambda)\sin(\theta)$, where λ is the wavelength of the X-rays and 2θ is the scattering angle) and the time delay t. The curves are averaged and normalized by scaling them to the absolute scale of the total (elastic and inelastic) scattering intensity from the nonexcited solvent/solute background in high q where the scattering is insensitive to structural changes. After normalization, the diffraction data for the unperturbed sample is subtracted from that collected at positive time delays to extract the diffraction change only. The difference diffraction intensities, $\Delta S(q,t)$, contain direct information about the structural changes of the solute and solvent in the probed solution. The relative laser-induced diffraction signal change, $\Delta S/S$, is quite small. It depends on both time and scattering angle and is typically

less than 0.1%. Standard deviations as a function of q are calculated in the process of conversion from a 2D image to a 1D curve by taking into account the distribution of the intensities at the same q value. The error of the averaged $\Delta S(q,t)$ can be obtained from the error propagation of standard deviations or by taking another standard deviation from the mean value of individual difference curves. The signal-to-noise ratio of a typical $\Delta S(q,t)$ depends on q and t and oscillates resembling the shape of $\Delta S(q,t)$ except that the negative values of $\Delta S(q,t)$ become positive in the plot of signal-to-noise ratio. A typical averaged $\Delta S(q,t)$ from about 50−100 repetitions has a signal-to-noise ratio up to 15. The signal-to-noise ratio is zero when ΔS is zero and reaches a maximum in the peaks and valleys of $\Delta S(q,t)$.

To emphasize the oscillatory feature at high q, $\Delta S(q,t)$ is often multiplied by q to yield $q\Delta S(q,t)$. Although $q\Delta S(q,t)$ contains direct information on the structural changes, often the result in the reciprocal space (q-space) is not intuitive, and for this reason, $q\Delta S(q,t)$ is transformed to real space where the changes are more readily interpretable: positive and negative peaks mean formation and depletion, respectively, of the corresponding interatomic distance. Obtained through sine-Fourier transforms of $q\Delta S(q,t)$, the difference radial distribution function, $r\Delta R(r,t)$ represents the experimental atom−atom pair distribution function during the course of the reaction[12−16]

$$r\Delta R(r, t) = \frac{1}{2\pi^2} \int_0^\infty q\Delta S(q, t) \sin(qr) \exp(-q^2\alpha) \, dq$$

where the constant α is a damping constant to account for the finite experimental q range. In principle, the errors in the r-space can be also obtained from the same procedure as the one described for the q-space data: The sine-Fourier transform of every single $q\Delta S(q,t)$ is taken and then averaged over all $r\Delta R(r,t)$ curves, which defines a meaningful standard deviation.

Data Analysis

We fit the experimental difference intensities ($\Delta S(q,t)_{\text{exp}}$) for all time delays against theoretical difference intensities ($\Delta S(q,t)_{\text{theory}}$) via a global fitting procedure simultaneously minimizing the difference between the experimental and theoretical curves at all positive time delays. The fitting parameters include the rate coefficients, the fraction of the excited molecules, and the fraction of the molecules undergoing structural changes. Structural parameters such as bond lengths, bond angles, and energy levels of chemical species can also be included as fitting parameters.
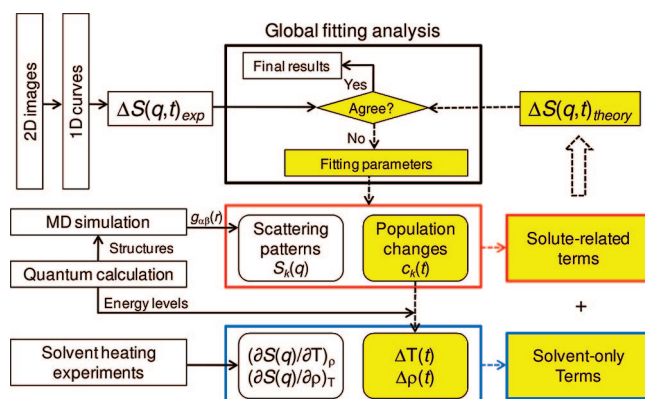
FIGURE 2. Schematic of the data analysis. The discrepancy between the theory and experiment is minimized using a global fitting analysis by considering data at all positive time delays simultaneously. Boxes with red and blue frames represent solute-related and solvent-only terms, respectively. Boxes with yellow background are involved in a typical iterative minimization procedure. See the text for details.

$\Delta S(q,t)_{\text{theory}}$ includes the changes from three principal components as shown in the following expression:

$$\Delta S(q, t)_{\text{theory}} = \Delta S(q, t)_{\text{solute-only}} + \Delta S(q, t)_{\text{solute−solvent}} + \Delta S(q, t)_{\text{solvent-only}}$$

$$= \Delta S(q, t)_{\text{solute-related}} + \Delta S(q, t)_{\text{solvent-only}}$$

$$= \left[\sum_k c_k(t)S_k(q) - S_g(q) \sum_k c_k(0) \right] + (\partial S / \partial T)_\rho \Delta T(t) + (\partial S / \partial \rho)_T \Delta \rho(t)$$

where k is the index of the solute (reactants, intermediates, and products), $c_k(t)$ is the fraction of molecules as a function of time t, $S_k(q)$ is the solute-related (the solute-only plus the cage components) scattering intensity of species k, $S_g(q)$ is the scattering intensity of the reactants (g = reactants), $(\partial S(q)/\partial T)_\rho$ is the solvent scattering change in response to a temperature rise at constant density, $(\partial S(q)/\partial \rho)_T$ is the response to a density change at constant temperature, and $\Delta T(t)$ and $\Delta \rho(t)$ are the solvent temperature and density changes as a function of time. The equation indicates that to calculate $\Delta S(q,t)_{\text{theory}}$, two types of basis components are needed (i.e., time-independent functions such as $S_k(q)$, $(\partial S(q)/\partial T)_\rho$, and $(\partial S(q)/\partial \rho)_T$ and time-dependent functions such as $c_k(t)$, $\Delta T(t)$, and $\Delta \rho(t)$). In the following, the steps involved in the calculation of time-independent and time-dependent basis functions are described. Figure 2 presents an overall scheme for data analysis.

The $S_k(q)$ are calculated from MD simulations combined with quantum calculations. After the MD simulations, pair correlation functions for atom pairs ($g_{\alpha\beta}(r)$ for the atom pair α and β) are calculated. The $S_k(q)$ curves are then computed by an equation including a sine Fourier transform of $g_{\alpha\beta}(r) - 1$. The

inclusion of $g_{\alpha\beta}(r)$ for only the pairs within the solute molecule results in the solute-only term, which can also be described by Debye scattering of isolated solute molecules in the gas phase. The cage term is calculated when the $g_{\alpha\beta}(r)$ for the solvent−solute cross pairs are used in the integration. In practice, $g_{\alpha\beta}(r)$ for both solute-only and solute−solvent cross pairs are used to yield the solute-only plus cage terms, that is, the solute-related terms, $S_k(q)$. The solvent differential functions, $(\partial S(q)/\partial T)_\rho$ and $(\partial S(q)/\partial\rho)_T$, can either be obtained by MD simulations or be determined in a separate experiment where the pure solvent is vibrationally excited by near-infrared light.[12] The latter gives superior agreement than the former does. In general, the $g_{\alpha\beta}(r)$ from MD simulation for a particular atom pair α and β can be used to calculate the contribution from that pair to the overall signal, thereby aiding the peak assignment.

The time-dependent basis functions ($c_k(t)$, $\Delta T(t)$, and $\Delta\rho(t)$) depend on the fitting parameters of the global fitting analysis. A set of rate equations for a reaction kinetic model including all reasonable candidate reaction pathways is set up to extract a reaction mechanism. Integrating the rate equations provides the $c_k(t)$ to be used to construct the theoretical scattering signal. The $\Delta T(t)$ and $\Delta\rho(t)$ are mathematically linked to $c_k(t)$ and to each other by energy and mass conservation and hydrodynamics. From $c_k(t)$, the time-dependent heat released from solutes to the solvent, $Q(t)$, is calculated, which is used to compute $\Delta T(t)$ and $\Delta\rho(t)$ via thermodynamic and hydrodynamics relations. The solvent can be heated by processes such as vibrational cooling occurring at a time scale too fast to be captured with the ~100 ps time resolution. The amount of heat caused by these processes is also included in $Q(t)$ by considering the fraction that enters these processes among the initially photoexcited species.

Figure 3A shows a comparison of $q\Delta S(q,t)_{\exp}$ and $q\Delta S(q,t)_{\text{theory}}$ from a global fitting analysis of TRXL data on HgI_2 in CH_3OH, and Figure 3B shows the corresponding $r\Delta R(r,t)_{\exp}$ and $r\Delta R(r,t)_{\text{theory}}$.[11] Figure 3E summarizes the final fit values. Upon irradiation of 10 mM HgI_2 in methanol, 33% ± 3% of the solute molecules are excited by the laser pulse at 267 nm. Among the excited HgI_2, 34% ± 1% dissociate into HgI + I within the time resolution of 100 ps, and the remaining 66% ± 4% decay into the ground state via vibrational cooling and release their energy to the solvent. Then 71% ± 1.2% of the transient HgI radicals recombine nongeminately with iodine atoms to form the parent molecule HgI_2 with a bimolecular rate constant of $(1.0 \pm 0.1) \times 10^{11}$ M^{-1} s^{-1}. The remaining 29% ± 0.5% of all iodine atoms combine to form I_2 with the rate constant $(3.3 \pm 0.5) \times 10^{10}$

M^{-1} s^{-1}. Based on these values from global fitting analysis, chemical population changes (as shown in Figure 3C) and the temperature and density change of the solvent (as shown in Figure 3D) as a function of time can be plotted. Initially, the temperature and the pressure of the solvent increase at constant density due to the energy transfer from the solute to solvent. Then a thermal expansion occurs with a time constant of ~50 ns, which returns the sample to ambient pressure. Due to the thermal expansion, the density of the solvent decreases by 0.83 kg/m^3 (0.1%) in 1 μs, which corresponds to a temperature increase of 0.71 K. After the analysis, the whole signal can be decomposed into each component. For example, the solute-only term, the cage term, and the solvent-only term in real space are shown in Figure 4D−F, along with assignment of the peaks in the real space. The prominent negative peaks around 2.65 and 5.30 Å of the solute-only term (Figure 4D) are mainly due to the depletion of the Hg−I and I···I distances in HgI_2.

Application Examples

A. Spatiotemporal Kinetics of HgI_2 in Methanol. Although numerous time-resolved spectroscopic studies had provided ample information about the early dynamics of HgI_2,[23,24] a comprehensive reaction mechanism in the solution phase spanning from picoseconds up to microseconds had been lacking. TRXL provided this information directly and quantitatively. Although HgI_2 has only three atoms, at least four different reaction channels need to be considered: (a) HgI + I, (b) Hg + I + I, (c) Hg + I_2, and (d) a HgI−I isomer. Figure 4A shows the comparison between $q\Delta S(q,100\text{ ps})_{\exp}$ and the corresponding fit results for the four candidate reaction channels. The two-body dissociation channel gave the best fit. Furthermore, when all reaction channels were included in the fit, the fraction of reaction channels except the two-body dissociation converged to zero, confirming that the formation of HgI + I is the dominant reaction pathway. The absence of the three-body dissociation into Hg + I + I is in contrast with the gas-phase dynamics where both two- and three-body dissociations were suggested to occur.[23] The subsequent kinetics obtained from TRXL is detailed in the previous section (Data Analysis).

B. Elimination Reaction of $C_2H_4I_2$ and $C_2F_4I_2$ in Methanol. We have applied TRXL to the elimination reaction of haloethanes, $C_2H_4I_2$ and its fluorine-substituted analogue $C_2F_4I_2$. Upon irradiation at 267 nm, both solute molecules dissociate into a haloethyl radical and an iodine atom. Of particular interest is the molecular structure of the haloethyl radical because a bridged structure rather than open
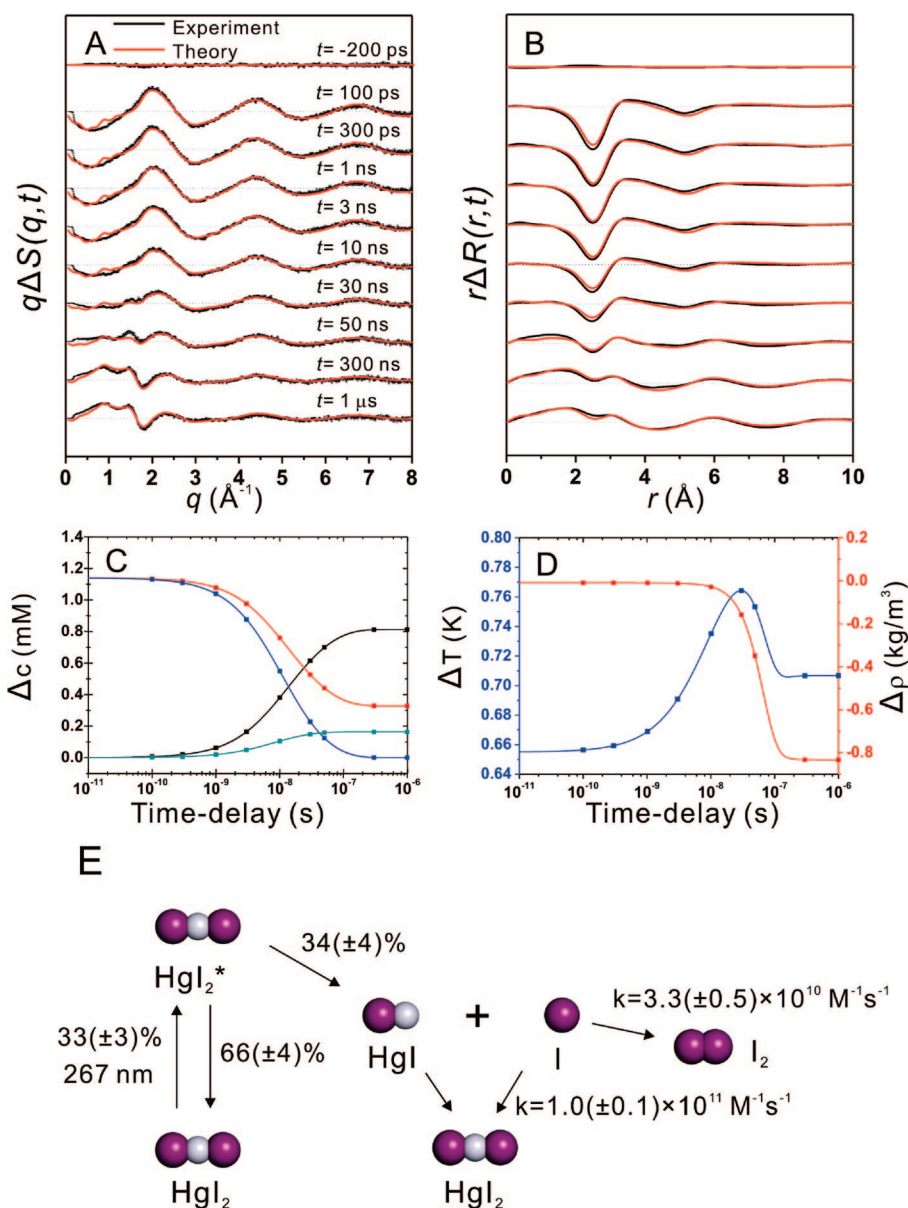
FIGURE 3. Structural dynamics of the photochemistry of HgI$_2$ in methanol upon photolysis at 267 nm determined by TRXL: (A) Experimental difference-diffraction intensities, $q\Delta S(q,t)$ (in black) with experimental errors and theoretical curves (in red) as a result of global fitting analysis; (B) difference radial distribution curves, $r\Delta R(r,t)$, corresponding to panel A; (C) the population changes of the various chemical species as a function of time delay determined from global fitting analysis; (D) the change in the solvent density (red) and temperature (blue) determined from global fitting analysis; (E) a reaction mechanism determined by TRXL.

classical structure (anti and gauche) had been proposed to explain the observed stereoselectivity of certain chemical processes[25] but had never been directly observed. The distinction between fits to the bridged and anti forms is emphasized when the contribution of the haloethyl radical (C$_2$H$_4$I or C$_2$F$_4$I) alone is carefully extracted by subtracting from the original data other contributions of solvent, cage, and other nascent solutes, and the high q range is used to deduce the transient-only structural changes. This approach allows the transient haloethyl radical to be modeled as a naked gas-phase structure. For the data at 100 ps, the experimental and theoreti-

cal curves for the putative reaction channels (Figure 5C,D) visually demonstrate that C$_2$H$_4$I has the bridged structure[10,26] whereas C$_2$F$_4$I is a mixture of anti and gauche conformers.[20] The negative peak near 5 Å corresponding to the depletion of the I···I internuclear distance in the parent molecule is common for both reaction channels leading to either bridged structure or classical structure, and both models agree with the data in this region. The peaks between 1 and 3 Å, the fingerprint region, are sensitive to the position of the I atom relative to the two carbon centers. A comparison of C$_2$H$_4$I and C$_2$F$_4$I provides a valuable chance to directly visualize the effect
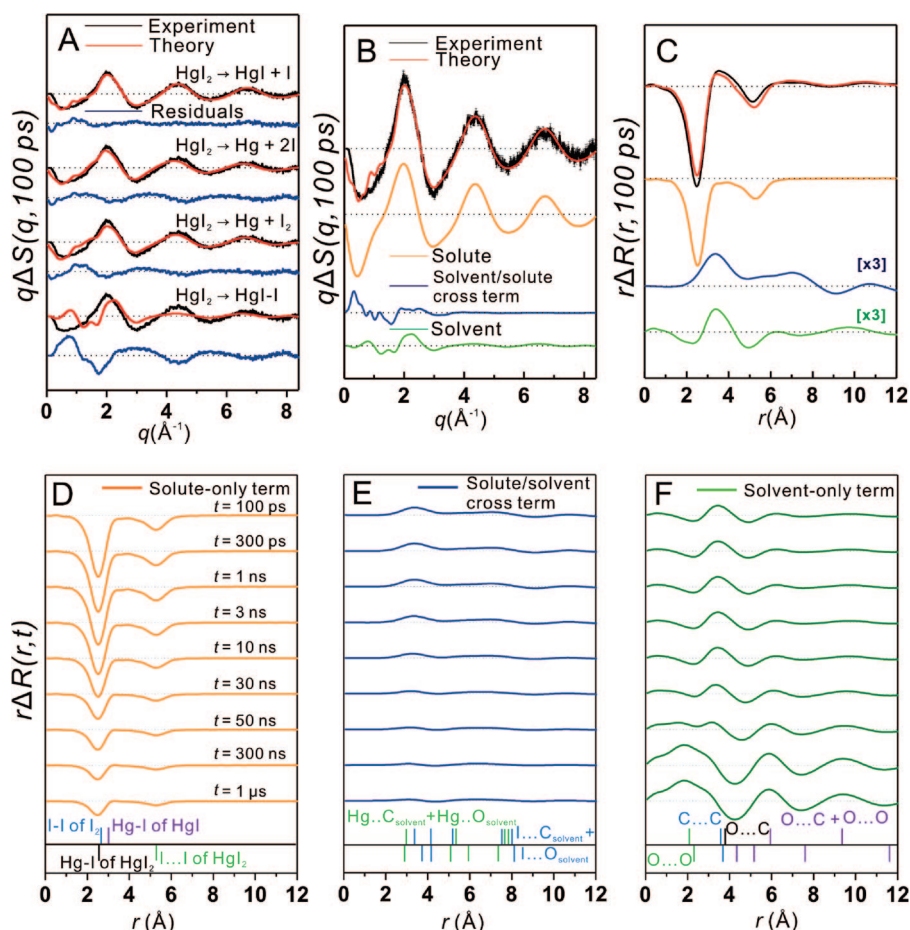
FIGURE 4. Determining the major reaction channel for HgI_2 in methanol excited at 267 nm and decomposition into three components for peak assignment: (A) $q\Delta S(q,100\ ps)$ for four candidate reaction pathways are compared. Experimental curves with experimental errors, theoretical curves and their differences (residuals) are shown in black, red, and blue, respectively. The two-body dissociation channel gives the best fit. (B) The $q\Delta S(q,100\ ps)$ curve is decomposed into the solute-only, cage, and solvent-only contributions. (C) The same decomposition in the real space for $r\Delta R(r,100\ ps)$ corresponding to panel B. (D) The solute-only component of $r\Delta R(r,t)$. (E) The cage component of $r\Delta R(r,t)$. (F) The solvent-only component of $r\Delta R(r,t)$. The peak assignments for atom−atom pairs are also shown in the bottom of each panel.

of fluorine substitution on the molecular structure of a radical. The reaction mechanisms also turn out to be completely different as summarized and compared in Figure 5A,B. The C_2H_4I radical does not decay through the formation of C_2H_4 + I; rather it reacts with an iodine atom to form a new species, the C_2H_4I−I isomer, with a bimolecular rate constant of $(2.1 \pm 0.3) \times 10^{12}\ M^{-1}\ s^{-1}$, which is larger by 2 orders of magnitude than the rate constant for nongeminate formation of molecular iodine. Eventually this isomer also decays into C_2H_4 + I_2 with the rate constant of $(4.8 \pm 0.9) \times 10^5\ s^{-1}$. By sharp contrast, $20\% \pm 1.3\%$ of the C_2F_4I radical decays into C_2F_4 + I with the time constant of 153 ± 24 ps. These values can be compared with the $55\% \pm 5\%$ and 26 ± 7 ps time constants determined from gas-phase ultrafast electron diffraction,[27] showing that the solvent reduces the rate and

yield of secondary dissociation significantly. No three-body dissociation to C_2F_4 + 2I is observed in the investigated time regime.

C. Structural Dynamics of $Ru_3(CO)_{12}$ in Cyclohexane. The triangular metal carbonyl cluster $Ru_3(CO)_{12}$ has served as the paradigm for the photochemistry of transition metal carbonyls. The complex is used as a catalyst in controlled photoactivated synthesis where specific types of bonds in the complex are broken at specific wavelengths. Because the mechanism leading to the cleavage of metal−metal bonds is of great theoretical and practical interest, the photolysis of $Ru_3(CO)_{12}$ had been extensively studied with spectroscopy. With the exception of ultrafast infrared spectroscopy, which has been most efficient in identifying intermediates based on the detection of bridging CO ligands, most techniques have
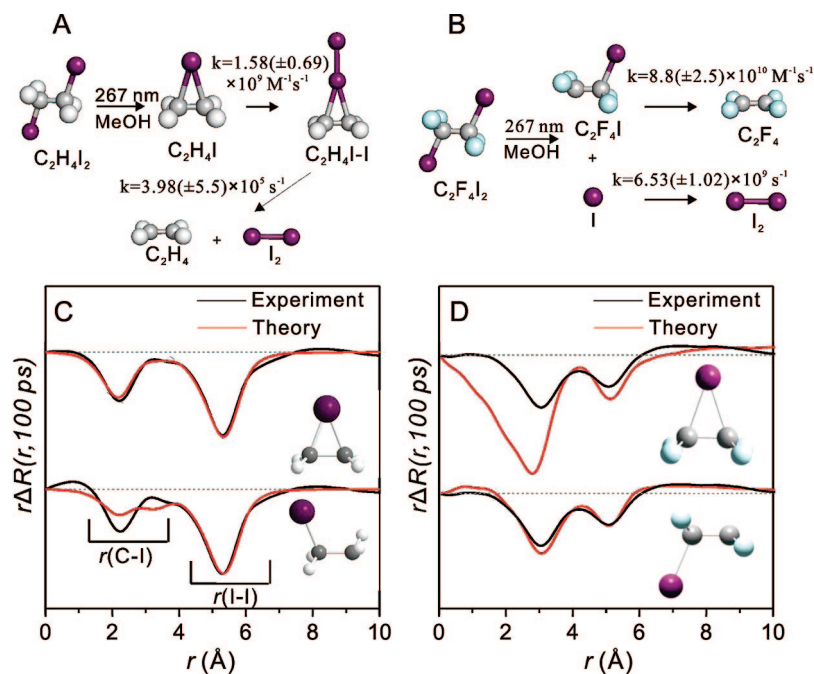
FIGURE 5. Structural dynamics of $C_2H_4I_2$ and its fluorine-substituted analogue $C_2F_4I_2$ in methanol excited at 267 nm determined by TRXL: (A) Reaction pathways for $C_2H_4I_2$; (B) reaction pathways for $C_2F_4I_2$; (C) theoretical (red) and experimental (black) $r\Delta R(r,100$ ps) for two possible reaction channels for $C_2H_4I_2$, the bridged radical (upper) versus an open radical (lower); the bridged structure gives superior agreement between theory and experiment; (D) the same comparison for $C_2F_4I_2$; the open classical structure gives superior agreement.

failed to characterize the structure of the intermediates. Recent ultrafast infrared spectroscopy measurements have shown that the photoexcited $Ru_3(CO)_{12}$ in noncoordinating solvents like cyclohexane yields two transient intermediates containing bridging carbonyls, $Ru_3(CO)_{11}(\mu\text{-CO})$ for the metal−metal cleavage reaction channel and $Ru_3(CO)_{10}(\mu\text{-CO})$ for the CO loss reaction channel, respectively.[28] We have applied TRXL to the photodissociation at a wavelength of 390 nm of $Ru_3(CO)_{12}$ dissolved in cyclohexane (shown in Figure 6A).[21] This system is one of the most complicated studied by TRXL because there are so many reaction channels that needed to be considered. Figure 6B shows the solute-only terms of the reaction channels considered in this work. The data analysis shows that the main photoproduct is one of the $Ru_3(CO)_{10}$ complex isomers with a Ru3-ring with terminal carbonyls only, which has a lifetime of tens of nanoseconds. The other $Ru_3(CO)_{10}$ isomers with bridging carbonyls do not match the time-resolved scattering data. The kinetics determined by TRXL is summarized in Figure 6C. Because the Ru−Ru distances contribute more than 90% of the scattering signal from the solute, an attempt has been made to optimize the initial DFT geometries of $Ru_3(CO)_{12}$ and the transient intermediates by refining a single scaling parameter applied to all Ru−Ru distances calculated by DFT. The optimized experimental bond lengths are shorter by a factor of 0.983 than those obtained by DFT, which is consistent with the general tendency for DFT to overestimate metal−metal distances.

D. Protein Structural Dynamics. In principle, TRXL should be possible for macromolecules such as proteins, but generally it is more difficult because proteins are at least a thousand times larger than typical small molecules and protein concentrations are lower. Due to the inverse relationship between the interatomic distance and the scattering angle, the scattering from macromolecules appears in smaller scattering angles (small-angle X-ray scattering or wide-angle X-ray scattering). Recently, promising TRXL data on prototype photoactive proteins in solution have been collected, and this methodology has been demonstrated.[29] Figure 7 shows an example for hemoglobin, a tetrameric protein made of two identical α/β dimers. A time-resolved X-ray scattering signal caused by the rotation of one dimer relative to the other dimer has been successfully detected. A preliminary kinetic analysis has suggested that the time scale for the quaternary change is slower than those from spectroscopy. Protein folding dynamics of cytochrome *c* has been also detected by TRXL. Detailed structural information such as the rotation angle and the subtle movements of α helices could not be directly extracted, and more development in this regard is in progress.
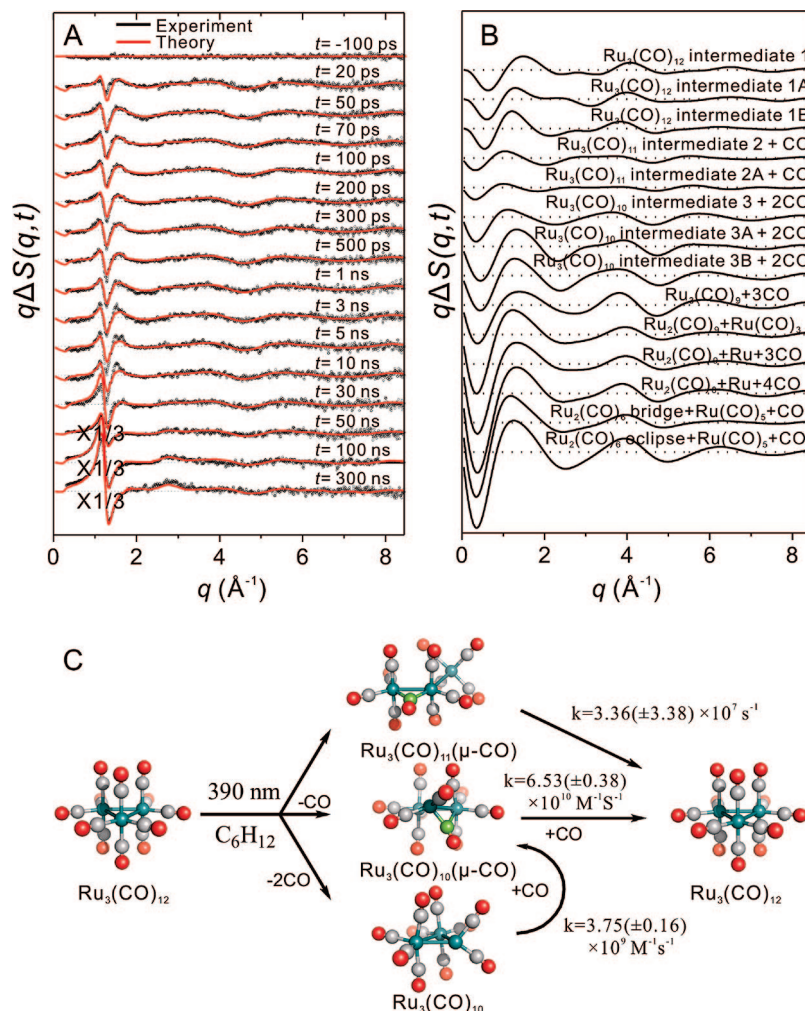
FIGURE 6. TRXL of $Ru_3(CO)_{12}$ in cyclohexane excited at 390 nm. (A) Time-resolved difference scattering intensities, $q\Delta S(q,t)$. The black curves correspond to the experimental data with experimental errors and the red curves to the theoretical least-squares fits (global fitting analysis). The values in the low q region of the first 13 curves and the last 3 curves have been divided by 3 and 6, respectively, for clarity. (B) Solute-only curves for all considered candidate reaction channels. (C) Reaction pathways for $Ru_3(CO)_{12}$ determined by global fitting analysis of TRXL data.

Concluding Remarks and Perspectives

TRXL offers a new and complementary method to probe reaction dynamics because it is sensitive to changes in the positions of all the atoms in the solution sample as a function of time. Molecular structures of all species along the reaction pathways including short-lived intermediates, their rate constants, and associated solvent hydrodynamics can be obtained. TRXL has been applied successfully to structural dynamics of small to macromolecules in solution. Most molecules studied so far contain atoms heavier than Br ($Z = 35$).[10−21] Applications to molecules without heavy atoms (for example, stilbene) may prove to be important for direct verification of reaction mechanisms in many photoinduced organic reactions but remain as a challenge due to the low contrast against the solvent. This low-contrast problem may be circumvented by labeling the solute molecule with heavy atoms or by using a solvent much heavier than the solute. Another challenge comes from macromolecules such as proteins. Although TRXL data has been successfully measured from protein solutions, extracting structural information by a proper analysis has not yet been fully accomplished. Development of data analysis should provide valuable information about protein structural dynamics including conformational transformation and folding/unfolding processes. The time resolution of TRXL is presently 100 ps, the limit imposed by the X-ray pulse length from a synchrotron. Due to this limited time resolution, ultrafast structural dynamics involved in ultrafast excited-state dynamics and direct observation of bond-breaking and -making processes cannot yet be accomplished with TRXL. This limit will be improved with future X-ray free elec-
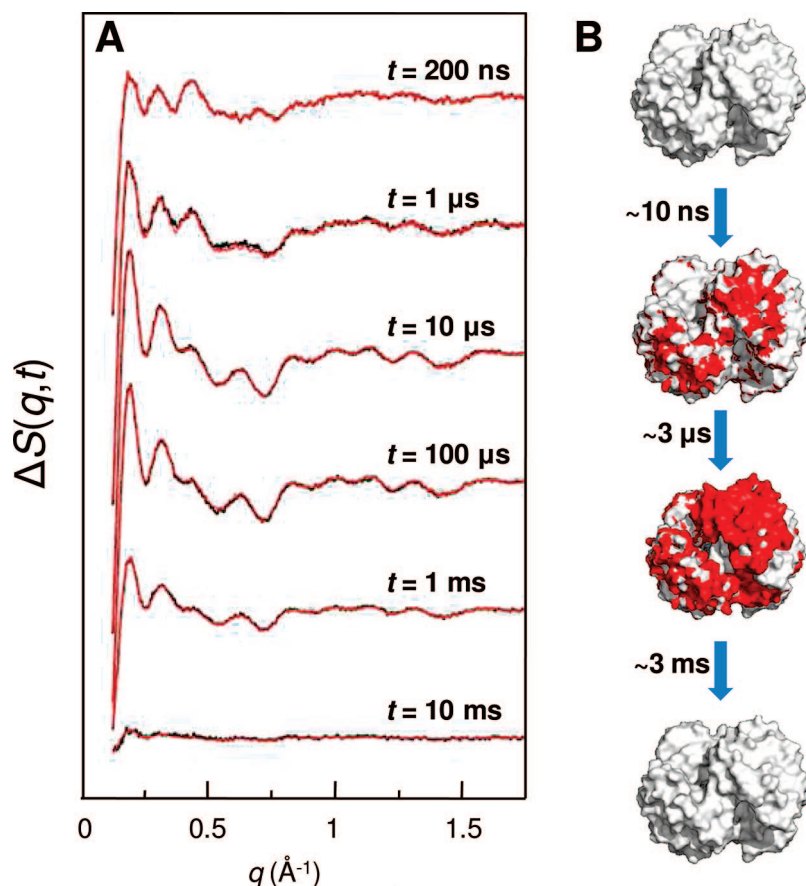
FIGURE 7. TRXL of hemoglobin in water excited at 532 nm. (A) Time-resolved difference scattering intensities, $\Delta S(q,t)$, at several representative time delays. Data (black curves) at all time delays can be well reproduced by a linear combination (red curves) of the difference patterns at 200 ns and 100 μs. (B) A schematic representation of the structural changes using low-resolution snapshots where white and red represent structures of the initial state and intermediates, respectively.

tron lasers (XFELs), which promise to deliver 100 fs long X-ray pulses with $\sim 10^{13}$ photons per pulse. In the current setup (detailed in the Experiment and Data Processing sections), a single diffraction image is a result of scattering 5 $\times 10^3$ X-ray pulses comprising $\sim 5 \times 10^{12}$ X-ray photons in total. Thus, a single-shot of the X-ray pulse from an XFEL source contains enough photons to generate a diffraction image comparable to an exposure of a few seconds using the third generation synchrotron source. This single-shot possibility should aid the synchronization between the laser excitation and the X-ray probe as each pair of the laser and X-ray pulses can be time stamped and thus the timing jitter can be essentially eliminated. It may be possible to take advantage of another important characteristic of XFEL X-ray pulses, high coherence, which can produce so-called speckles in the diffraction pattern. The real challenge with XFEL may come from the data analysis. In the current data analysis of TRXL data with 100 ps time resolution, the X-ray scattering pattern can be approximated to depend only on a one-dimensional scalar quantity q rather than the two-

dimensional vector **q** since 100 ps is long enough. In addition, the scattering patterns could be well represented by considering equilibrium structures. These approximations may no longer be valid if the time resolution is improved 1000-fold. In summary, many exciting challenges and opportunities are waiting to be discovered.

BIOGRAPHICAL INFORMATION

Hyotcherl Ihee received his undergraduate degree at KAIST in 1994 and obtained a Ph.D. degree at Caltech in 2001. As a graduate student with Prof. Ahmed Zewail, he contributed to the development of ultrafast electron diffraction. For his postdoctoral

work with Prof. Keith Moffat at the University of Chicago, he studied protein structural dynamics by using time-resolved X-ray crystallography. After joining the faculty at KAIST in 2003, he has contributed to the advancement of TRXL. His research interests include molecular structural and chemical reaction dynamics investigated with time-resolved X-ray/electron diffraction (scattering) and spectroscopy.

REFERENCES

1 Zewail, A. H. Femtochemistry: Atomic-scale dynamics of the chemical bond using ultrafast lasers (Nobel lecture). *Angew. Chem., Int. Ed.* **2000**, *39*, 2586–2631.

2 Kao, Y. T.; Saxena, C.; Wang, L. J.; Sancar, A.; Zhong, D. P. Direct observation of thymine dimer repair in DNA by photolyase. *Proc. Natl. Acad. Sci. U.S.A.* **2005**, *102*, 16128–16132.

3 Kukura, P.; McCamant, D. W.; Yoon, S.; Wandschneider, D. B.; Mathies, R. A. Structural observation of the primary isomerization in vision with femtosecond-stimulated Raman. *Science* **2005**, *310*, 1006–1009.

4 Mizutani, Y.; Kitagawa, T. Direct observation of cooling of heme upon photodissociation of carbonmonoxy myoglobin. *Science* **1997**, *278*, 443–446.

5 Lee, H.; Cheng, Y. C.; Fleming, G. R. Coherence dynamics in photosynthesis: Protein protection of excitonic coherence. *Science* **2007**, *316*, 1462–1465.

6 Zheng, J. R.; Kwak, K. W.; Xie, J.; Fayer, M. D. Ultrafast carbon-carbon single-bond rotational isomerization in room-temperature solution. *Science* **2006**, *313*, 1951–1955.

7 Collet, E.; Lemee-Cailleau, M. H.; Buron-Le Cointe, M.; Cailleau, H.; Wulff, M.; Luty, T.; Koshihara, S. Y.; Meyer, M.; Toupet, L.; Rabiller, P.; Techert, S. Laser-induced ferroelectric structural order in an organic charge-transfer crystal. *Science* **2003**, *300*, 612–615.

8 Tomov, I. V.; Oulianov, D. A.; Chen, P. L.; Rentzepis, P. M. Ultrafast time-resolved transient structures of solids and liquids studied by means of X-ray diffraction and EXAFS. *J. Phys. Chem. B* **1999**, *103*, 7081–7091.

9 Vorontsov, I. I.; Kovalevsky, A. Y.; Chen, Y. S.; Graber, T.; Gembicky, M.; Novozhilova, I. V.; Omary, M. A.; Coppens, P. Shedding light on the structure of a photoinduced transient excimer by time-resolved diffraction. *Phys. Rev. Lett.* **2005**, *94*, 193003.

10 Ihee, H.; Lorenc, M.; Kim, T. K.; Kong, Q. Y.; Cammarata, M.; Lee, J. H.; Bratos, S.; Wulff, M. Ultrafast X-ray diffraction of transient molecular structures in solution. *Science* **2005**, *309*, 1223–1227.

11 Kim, T. K.; Lorenc, M.; Lee, J. H.; Russo, M. L.; Kim, J.; Cammarata, M.; Kong, Q.; Noel, S.; Plech, A.; Wulff, M.; Ihee, H. Spatiotemporal reaction kinetics of an ultrafast photoreaction pathway visualized by time-resolved liquid X-ray diffraction. *Proc. Natl. Acad. Sci. U.S.A.* **2006**, *103*, 9410–9415.

12 Cammarata, M.; Lorenc, M.; Kim, T. K.; Lee, J. H.; Kong, Q. Y.; Pontecorvo, E.; Russo, M. L.; Schiro, G.; Cupane, A.; Wulff, M.; Ihee, H. Impulsive solvent heating probed by picosecond X-ray diffraction. *J. Chem. Phys.* **2006**, *124*, 124504.

13 Plech, A.; Wulff, M.; Bratos, S.; Mirloup, F.; Vuilleumier, R.; Schotte, F.; Anfinrud, P. A. Visualizing chemical reactions in solution by picosecond X-ray diffraction. *Phys. Rev. Lett.* **2004**, *92*, 125505.

14 Wulff, M.; Bratos, S.; Plech, A.; Vuilleumier, R.; Mirloup, F.; Lorenc, M.; Kong, Q.; Ihee, H. Recombination of photodissociated iodine: A time-resolved X-ray-diffraction study. *J. Chem. Phys.* **2006**, *124*, 034501.

15 Davidsson, J.; Poulsen, J.; Cammarata, M.; Georgiou, P.; Wouts, R.; Katona, G.; Jacobson, F.; Plech, A.; Wulff, M.; Nyman, G.; Neutze, R. Structural determination of a transient isomer of CH_2I_2 by picosecond X-ray diffraction. *Phys. Rev. Lett.* **2005**, *94*, 245503.

16 Lee, J. H.; Kim, K. H.; Kim, T. K.; Lee, Y.; Ihee, H. Analyzing solution-phase time-resolved X-ray diffraction data by isolated-solute models. *J. Chem. Phys.* **2006**, *125*, 174504.

17 Wulff, M.; Bratos, S.; Plech, A.; Vuilleumier, R.; Mirloup, F.; Lorenc, M.; Kong, Q.; Ihee, H. Recombination of photo-dissociated iodine: A time-resolved X-ray diffraction study. *J. Chem. Phys.* **2006**, *124*, 034501.

18 Kong, Q. Y.; Wulff, M.; Lee, J. H.; Bratos, S.; Ihee, H. Photochemical reaction pathways of carbon tetrabromide in solution probed by picosecond X-ray diffraction. *J. Am. Chem. Soc.* **2007**, *129*, 13584–13591.

19 Lee, J. H.; Kim, J.; Cammarata, M.; Kong, Q.; Kim, K. H.; Choi, J.; Kim, T. K.; Wulff, M.; Ihee, H. Transient X-ray diffraction reveals global and major reaction pathways for the photolysis of iodoform in solution. *Angew. Chem., Int. Ed.* **2008**, *47*, 1047–1050.

20 Lee, J. H.; Kim, T. K.; Kim, J.; Kong, Q.; Cammarata, M.; Lorenc, M.; Wulff, M.; Ihee, H. Capturing transient structures in the elimination reaction of haloalkane in solution by transient X-ray diffraction. *J. Am. Chem. Soc.* **2008**, *130*, 5834–5835.

21 Kong, Q.; Lee, J. H.; Plech, A.; Wulff, M.; Ihee, H.; Koch, M. H. J. Ultrafast X-ray solution scattering reveals an unknown reaction intermediate in the photolysis of $Ru_3(CO)_{12}$. *Angew. Chem., Int. Ed.* **2008**, *47*, 5550–5553.

22 Ihee, H.; Rajagopal, S.; Srajer, V.; Pahl, R.; Anderson, S.; Schmidt, M.; Schotte, F.; Anfinrud, P. A.; Wulff, M.; Moffat, K. Visualizing reaction pathways in photoactive yellow protein from nanoseconds to seconds. *Proc. Natl. Acad. Sci. U.S.A.* **2005**, *102*, 7145–7150.

23 Zhong, D.; Zewail, A. H. Femtosecond real-time probing of reactions. 23. Studies of temporal, velocity, angular, and state dynamics from transition states to final products by femtosecond-resolved mass spectrometry. *J. Phys. Chem. A* **1998**, *102*, 4031–4058.

24 Pugliano, N.; Szarka, A. Z.; Hochstrasser, R. M. Relaxation of the product state coherence generated through the photolysis of HgI_2 in solution. *J. Chem. Phys.* **1996**, *104*, 5062–5079.

25 Skell, P. S.; Tuleen, D. L.; Readio, P. D. Stereochemical evidence of bridged radicals. *J. Am. Chem. Soc.* **1963**, *85*, 2849–2850.

26 Cao, J.; Ihee, H.; Zewail, A. H. Ultrafast electron diffraction and direct observation of transient structures in a chemical reaction. *Proc. Natl. Acad. Sci. U.S.A.* **1999**, *96*, 338–342.

27 Ihee, H.; Lobastov, V. A.; Gomez, U. M.; Goodson, B. M.; Srinivasan, R.; Ruan, C. Y.; Zewail, A. H. Direct imaging of transient molecular structures with ultrafast diffraction. *Science* **2001**, *291*, 458–462.

28 Glascoe, E. A.; Kling, M. F.; Shanoski, J. E.; Harris, C. B. Nature and role of bridged carbonyl intermediates in the ultrafast photoinduced rearrangement of $Ru_3(CO)_{12}$. *Organometallics* **2006**, *25*, 775–784.

29 Cammarata, M.; Levantino, M.; Schotte, F.; Anfinrud, P. A.; Ewald, F.; Choi, J.; Cupane, A.; Wulff, M.; Ihee, H. Tracking the structural dynamics of proteins in solution using time-resolved wide-angle X-ray scattering. *Nat. Methods* **2008**, *5*, 881–886.